Univerza *v Ljubljani*

Seminar Ib

Lensfree Microscopy and Digital Holography

Author:
Jošt Stergar

Consultant:
dr. Natan Osterman

Academic year 2014/2015

Abstract

Lensfree microscopy is a derivative method of a more general digital holography, where interference pattern of light, e.g. hologram, is digitally captured and then used to numerically reconstruct the real image. The numerical reconstruction is generally performed using algorithms employing the effective fast Fourier transformation (FFT) as their core component. This novel method can be used to produce inexpensive devices with high resolution, high magnification and unprecedented field of view. Devices and methods range from ultra-portable on-the-field cellphone digital holographic microscopes to Pixel SuperResolution devices with subpixel reconstruction for quality of resulting images close to that of classical optical microscopes, without the added bulk of optical equipment. Some research on applicative aspects of said devices has been made in the last years, showing promising results for their general use.

Table of Contents

1 Introduction

The idea of lensfree or digital holographic microscopy has been around for quite some time [1], but recent advancements in the production of low-cost imaging sensors and higher availability of processing power have enabled research of new methods [2].

Classical microscopy is a time-tested method for observing small samples, but its main drawback is bulky and unportable equipment. Also, lenses and other materials needed for production of classical microscopes are quite expensive, making them inaccessible to some developing countries. Lensfree microscopy does not require such bulky equipment, rather it needs only a detection element, commonly a CCD or CMOS sensor, and moderate processing power. Both components can be found in most modern-day smartphones and are relatively inexpensive and easy to manufacture. The advantage of this method is thus lack of any optical equipment which is replaced by numerical reconstruction algorithms. Some information is obviously lost in the process of image reconstruction, but the final resolution can be quite usable [2], ranging to a few microns. The resolution can be enhanced by modifying the reference beam, an example of such method is Pixel SuperResolution developed by Ozcan and coworkers [3]. Another advantage of lensfree microscopy over its classical counterpart is its field of view size which becomes increasingly important when dealing with modern lab-on-a-chip (LOC) devices. A large field of view enables monitoring of whole segments of LOC devices with one simple sensor, without the need for bulky devices and complicated translation elements. Moreover, it is possible to build LOC devices which have microscope elements already built in, thus opening horizons for many novel applications.

In this seminar we firstly take a look at the area of digital holography in par-axial approximation, which will enable us to derive the Fresnel transformation using Fresnel approximation. This will give us a basic understanding of the numerical algorithms used for amplitude and phase reconstruction, two important problems of digital holography. We will then establish digital holographic microscopy (DHM) or lensfree microscopy as a derivation of said technique. Armed with this knowledge, we will look at some of the basic designs of DHM, such as a cellphone lensfree microscope. For conclusion we will examine some examples of DHM use in realistic biological applications.

2   Digital Holography

Digital holography is a general term covering different ranges from digital production to reconstruction of holograms. We will focus on the latter and firstly examine different methods that enable reconstruction of an image of scatterers from their interferogram, as recorded by a sensor in way of a digital hologram.

The whole approach of digital holography is based on the fact that each spot in a hologram, described by the hologram function $h(x, y)$, interacts with the reference wave $R(x, y)$, giving a response in accordance with its response function $g(x, y, \xi, \eta)$. To write the response function, every point is treated as an aperture. To recover complex amplitude in one spot on the reconstruction plane, the response of a whole system must be taken into the account with a double integral over the hologram plane. Full complex amplitude at the reconstruction plane $\Gamma(\xi, \eta)$ can then be written in the form [4]:

$$\Gamma(\xi, \eta) = \int_{-\infty}^{\infty} \int_{-\infty}^{\infty} h(x, y) R(x, y) g(\xi - x, \eta - y) \mathrm{d}x \mathrm{d}y, \tag{1}$$

or with the response function written out

$$\Gamma(\xi, \eta) = \frac{i}{\lambda} \int_{-\infty}^{\infty} \int_{-\infty}^{\infty} h(x, y) R(x, y) \frac{e^{-i\frac{2\pi}{\lambda}\rho}}{\rho} \left(\frac{1}{2} + \frac{1}{2}\cos\theta \right) \mathrm{d}x \mathrm{d}y, \tag{2}$$

where coordinate systems and other quantites are defined in Figure 1 below. This equation is sometimes known as the *Fresnel-Kirchoff integral*.
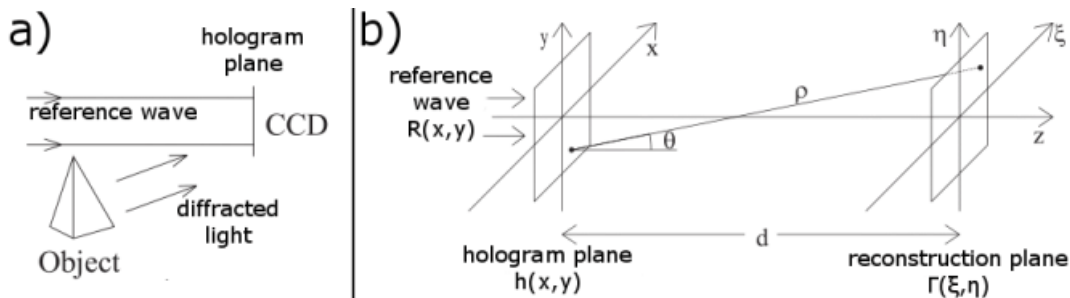

Figure 1: ***Recording and reconstruction of holograms.*** *To record a hologram, the reference beam interferes with the light that is diffracted from the observed object. The image is captured using a sensor positioned in the hologram plane, as shown in figure a). When reconstructing the image as shown in figure b), two separate coordinate systems are set up. The first coordinate system is in the plane of the recorded hologram, and uses coordinates x, y. A second coordinate system is positioned in the plane of the reconstructed image, using coordinates ξ, η. The hologram and the reconstruction plane are separated by distance d. The separation between points in both planes is defined as ρ and its deviation from the optical axis by angle θ [4].*

This equation does not reconstruct light intensity in the object plane, but rather intensity in the reconstruction plane, positioned behind the hologram plane and object plane. To obtain a real image, as it would be seen by the naked eye in the reconstruction plane, a proper focusing lens has to be introduced [4]. This lens is placed immediately behind the hologram plane, as shown in Figure 2. Numerical representation of this lens is given by

$$L(x, y) = e^{i\frac{\pi}{\lambda f}(x^2 + y^2)}, \tag{3}$$

with its focal length set at $f = d/2$ to achieve unit magnification in the reconstruction plane.

For further computations, lens equation (3) is multiplied into the Fresnel-Kirchoff integral (1) or (2).

With calculated complex amplitude, the phase of light and its real amplitude at the reconstruction plane are simply calculated as [4]

$$\phi(\xi, \eta) = \arctan \frac{\Im\{\Gamma(\xi, \eta)\}}{\Re\{\Gamma(\xi, \eta)\}}, \tag{4}$$

and its amplitude

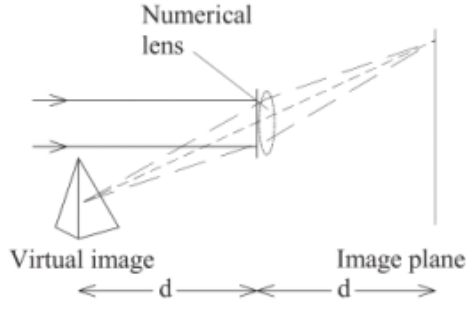$$I(\xi, \eta) = |\Gamma(\xi, \eta)|^2. \tag{5}$$

Figure 2: **Numerical lens.** *Because holograms only record and reconstruct interference of reference and scattered light in the hologram plane, they do not focus light and create a real image in some focal plane, when direction of the beam is same as when recording the hologram; the image is thus virtual. To reconstruct a real image, the direction of laser beam has to be reversed, or a numerical representation of an eye lens has to be introduced into the equation. This lens is placed directly behind the hologram plane. To achieve unit magnification, the focal distance of the lens has to be set at $d/2$, in which case the image plane coincides with the reconstruction plane [4].*

2.1 Fresnel approximation

The Fresnel-Kirchoff equation (2) is difficult to evaluate directly, so some approximations have to be introduced, namely Taylor expansion, to transform into a form which can be evaluated by means of a modified fast Fourier transform (FFT), sometimes called the Fresnel transformation [4]. First we expand distance ρ between points in the reconstruction and hologram planes for small differences in $(\xi - x)$ and $(\eta - y)$ to the second order

$$\rho = \sqrt{d^2 + (x - \xi)^2 + (y - \eta)^2} \approx d + \frac{(\xi - x)^2}{2d} + \frac{(\eta - y)^2}{2d} + \dots \tag{6}$$

Then, we approximate the cosine of angle θ using $\cos\theta \approx 1$, taking into account small deviations from the optical axis. Furthermore, we approximate distance ρ in denominator in (2) to the first order of its Taylor expansion with $\rho \approx d$, thus obtaining

$$\Gamma(\xi, \eta) = \frac{i}{\lambda d} e^{-i\frac{2\pi}{\lambda}d} \int_{-\infty}^{\infty} \int_{-\infty}^{\infty} R(x, y) h(x, y) e^{-i\frac{\pi}{\lambda d}((\xi - x)^2 + (\eta - y)^2)} \mathrm{d}x \mathrm{d}y. \tag{7}$$

Executing the multiplication under the integral leaves us with

$$\Gamma(\xi, \eta) = \frac{i}{\lambda d} e^{-i\frac{2\pi}{\lambda}d} e^{-i\frac{\pi}{\lambda d}(\xi^2 + \eta^2)} \int_{-\infty}^{\infty} \int_{-\infty}^{\infty} R(x, y) h(x, y) e^{-i\frac{\pi}{\lambda d}(x^2 + y^2)} e^{-i\frac{2\pi}{\lambda d}(x\xi + y\eta)} \mathrm{d}x \mathrm{d}y. \tag{8}$$

Since this form would not reconstruct a real image, we must at this point introduce a numerical lens, positioned so as to give unit image magnification. To this end, we multiply lens factor (3) into equation (8). As it turns out, only sign in one of the exponentials flips, leaving us with the equation

$$\Gamma(\xi, \eta) = \frac{i}{\lambda d} e^{-i\frac{2\pi}{\lambda}d} e^{-i\frac{\pi}{\lambda d}(\xi^2 + \eta^2)} \int_{-\infty}^{\infty} \int_{-\infty}^{\infty} R(x, y) h(x, y) e^{+i\frac{\pi}{\lambda d}(x^2 + y^2)} e^{-i\frac{2\pi}{\lambda d}(x\xi + y\eta)} \mathrm{d}x \mathrm{d}y. \tag{9}$$

2.1.1 Discrete Fresnel transformation

Since CCD or CMOS sensors consist of finite-sized sensing cells, hologram data is also discrete. Thus discrete method to calculate a real image in the reconstruction plane must be developed. It is also desirable to translate the problem of calculating equation (9) to some other problem that is easily solvable, namely the Fourier transformation. To this end, we first introduce two new variables

$$\nu = \frac{\xi}{\lambda d}, \qquad\qquad \mu = \frac{\eta}{\lambda d}. \tag{10}$$

Omitting the first exponential factor in equation (9), since it contributes only to the overall phase, and introducing this new set of variables leaves us with the equation of form

$$\Gamma(\nu, \mu) = \frac{\mathrm{i}}{\lambda d} e^{-\mathrm{i}\pi\lambda d(\nu^2 + \mu^2)} \int_{-\infty}^{\infty} \int_{-\infty}^{\infty} R(x, y) h(x, y) e^{+\mathrm{i}\frac{\pi}{\lambda d}(x^2 + y^2)} e^{\mathrm{i}2\pi(x\nu + y\mu)} \mathrm{d}x \mathrm{d}y. \tag{11}$$

Comparing equation (11) to the definition of the 2D Fourier transformation, it is easy to see, that

$$\Gamma(\nu, \mu) = \frac{\mathrm{i}}{\lambda d} e^{+\mathrm{i}\pi\lambda d(\nu^2 + \mu^2)} \mathcal{F}^{-1}\left[R(x, y) h(x, y) e^{-\mathrm{i}\frac{\pi}{\lambda d}(x^2 + y^2)} \right]. \tag{12}$$

At this point, the only problem left is the discretization of this equation. Given a discrete reference image $R(k,l)$ and a hologram $h(k,l)$ we can rewrite integral (11) into a discrete form

$$\Gamma(m,n) = \frac{\mathrm{i}}{\lambda d} e^{-\mathrm{i}\pi\lambda d(m^2\Delta\nu^2 + n^2\Delta\mu^2)} \sum_{k=0}^{N-1}\sum_{l=0}^{N-1} R(k,l)h(k,l) e^{+\mathrm{i}\frac{\pi}{\lambda d}(k^2\Delta x^2 + l^2\Delta y^2)} e^{\mathrm{i}2\pi(k\Delta x m\Delta\nu + l\Delta y n\Delta\mu)}, \quad (13)$$

where the summation in k,l runs over the whole recorded image of size $N \times N$, and $\Delta x, \Delta y$ is the separation between the pixels of a detector. Using the relations for discrete Fourier transform [4]

$$\Delta\nu = \frac{1}{N\Delta x}, \qquad\qquad \Delta\mu = \frac{1}{N\Delta y}, \qquad (14)$$

we write the final form of the *discrete Fresnel transformation*

$$\Gamma(m,n) = \frac{\mathrm{i}}{\lambda d} e^{-\mathrm{i}\pi\lambda d\left(\frac{m^2}{N^2\Delta x^2} + \frac{n^2}{N^2\Delta y^2}\right)} \sum_{k=0}^{N-1}\sum_{l=0}^{N-1} \left[R(k,l)h(k,l) e^{+\mathrm{i}\frac{\pi}{\lambda d}(k^2\Delta x^2 + l^2\Delta y^2)} \right] e^{\mathrm{i}2\pi\left(\frac{km}{N} + \frac{ln}{N}\right)}. \quad (15)$$

The complex amplitude is thus easily calculated by evaluating the part of expression (15) in the square brackets and performing the FFT on the resulting matrix. The recorded hologram and its reconstruction using the described algorithm is shown in Figure 3. This set of images also demonstrates that every part of a hologram contains information about the whole object being recorded. Decreasing the sample size simply limits the viewfield of the reconstruction, as shown by the rightmost part of the image. In these images a central bright square which is actually an image of the undiffracted reference beam can be seen. This part can be removed but discussion of its suppression does not serve our goal of understanding digital holographic microscopy.
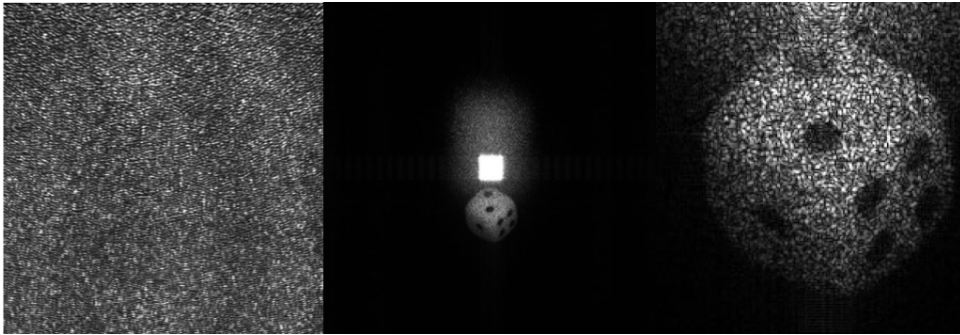

Figure 3: **Digital hologram and image reconstruction.** *The first image represents recorded intensities in the hologram plane on a CCD device. The second image is a reconstruction of a full hologram. The third image demonstrates some of the more eccentric properties of holograms; if only a quarter of data from the CCD is taken, the central part of the image is again reconstructed, but the overall field of view is decreased, as though we were watching through a smaller window. The bright central square in the image is the reference beam that has not been removed [4].*

2.2 Convolution method

When we want to use digital holography to record microscopic images, it is desirable to achieve a high spatial resolution. To do this, a sample must be moved relatively close to the sensor [4], thus breaking the approximation made in the previous section. The Fresnel approximation does not hold anymore and a different approach has to be used.

Equation (1) has the form of a convolution, so the convolution theorem can be used, giving the equation

$$\Gamma(\xi,\eta) = \mathcal{F}^{-1}\{\mathcal{F}(h(x,y)R(x,y))\mathcal{F}(g)\}. \qquad (16)$$

The Fourier transformation of the Green's function g can be calculated beforehand $G = \mathcal{F}(g)$, thus saving one Fourier transformation

$$\Gamma(\xi,\eta) = \mathcal{F}^{-1}\{\mathcal{F}(h(x,y)R(x,y))G(k,l)\}. \qquad (17)$$

This generalized approach is suitable for more applications than the Fresnel transformation (15), since it does not contain any special assumptions about the Green's function, and can be used to reconstruct digital holographic microscopy images.

3 Lensfree Microscopy devices

This second part of the seminar examines two different applications of digital holographic microscopy in accordance with the reconstruction theory presented in the previous part. Depending on the desired properties of a final device, different setups can be developed. Distinct advanced methods can be used to, for example, increase the resolution of the final image, as is the case with the experimental setup described in the second subsection. Simple, inexpensive and highly portable devices for on-field usage, such as the cellphone digital holographic microscope, can also be implemented using the above mentioned methods.

3.1 Digital Holographic microscope with Pixel SuperResolution

The limiting factor of resulting images, recorded using digital holography methods, is the pixel size which effectively limits the possible magnification, e.g. its spatial resolution. To increase the image resolution without decreasing the sensor pixel size and consequently diminishing its sensitivity, a novel approach that allows to effectively increase hologram resolution has been developed.

In the described approach, multiple lower resolution holograms are combined. To reconstruct details smaller than the physical pixel size, the source of light is moved, causing subpixel changes in the fringe pattern on the hologram plane. Using an iterative algorithm these images are later combined, forming one super resolved image [3].

A simple setup consists of a sensor which serves to detect the holographic pattern, and a movable pinhole, as shown in figure 4.
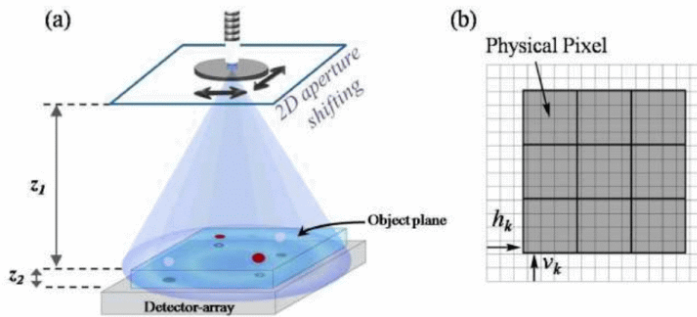

Figure 4: **Pixel SuperResolution setup.** *This novel setup is based on in-line partially coherent holography, with the addition of a movable source. Reconstruction using a special algorithm can increase the resolution of the final hologram over the one defined by the sensor size and the physical pixel size. In this way, the quality of the produced images can be significantly increased [3].*

To better understand the inner workings of the Pixel SuperResolution method, we shall first examine what the relation between the value of a physical pixel and virtual subpixels is. A grid of physical pixels and its enhanced resolution counterparts is shown in Figure 4. The value of the physical pixel is simply a weighted average of subpixels. We denote the higher resolution image with the vector $\mathbf{Y} = [y_1, y_2, ..., y_N]$ and the k-th lower resolution image by $\mathbf{X_k} = [x_{k,1}, x_{k,2}, ..., x_{k,M}]$, thus obtaining the formula for a calculated pixel of lower resolution image $\tilde{x}_{k,j}$ as

$$\tilde{x}_{k,j} = \sum_{i=1}^{N} W_{k,i,j}(h_k, v_k) y_i, \tag{18}$$

where $W_{k,i,j}(h_k, v_k)$ is some weighting constant that depends on the position of the reference beam pinhole h_k and v_k. The higher resolution image is then obtained by iterative numerical minimization of cost function

$$C(\mathbf{Y}) = \frac{1}{2} \sum_{k=1...p, i=1...M} (x_{k,i} - \tilde{x}_{k,i})^2 + \frac{\alpha}{2} \mathbf{Y}_{filtered}^T \mathbf{Y}_{filtered}, \tag{19}$$

where the first term is a simple difference of calculated and measured pixels. The first sum runs over all of the lower resolution images, while the other runs over all the pixels in one such image. The second term is slightly more complicated and it represents a high frequency suppression term, since the first term in the cost function is susceptible to a high frequency noise. In this term, $\mathbf{Y}_{filtered}$ represents a high-pass filtered reconstruction candidate. This term penalizes the high frequency noise of the method. Coefficient α is chosen so that the noise is eliminated well. In the setup described here, the coefficient is simply $\alpha = 1$.

The only remaining problem is the calculation of the weighting coefficient $W_{k,i,j}(h_k, v_k)$. In the work presented here, it is assumed that $W_{k,i,j}$ coefficients are determined by the 2D light sensitivity map of the sensor.

When multiple lower resolution images (Figure 5a) are combined according to the described algorithm, a higher resolution image is obtained (Figure 5c). In this pixel super resolved hologram even finer interference fringes can be seen, as demonstrated by magnification of the area in Figure 5c. In the described algorithm such weighting coefficients can be used that the path, depicted in Figure 5b, is self-calibrating, thus eliminating the need for precision mechanics and reducing the overall cost of the setup.
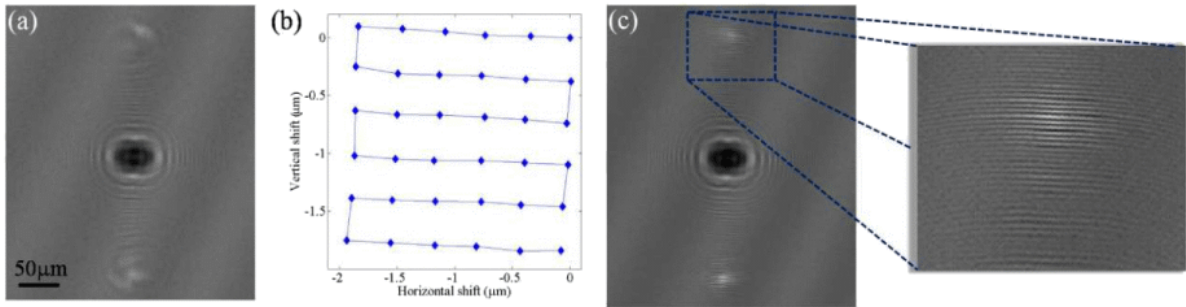

Figure 5: **Pixel SuperResolution and normal resolution hologram comparison.** *As example of the Pixel SR normal resolution images and enhanced images are compared. This enhancement is achieved by moving the aperture of the system along the path, outlined in figure b. Upon closer examination, finer interference fringes which are indistinguishable in the normal resolution image, can be observed in the enhanced version [3].*

With this method, the reconstruction of high spatial resolution images over a wide field of view is possible. Excerpts from a larger digital holographic microscopy image are gathered and compared to lower resolution reconstructions and optical microscope images in figure 6. A clear improvement over the lower resolution reconstructions is visible, with the quality of Pixel SR images approaching that of an optical microscope, with subcellular structures clearly resolvable.
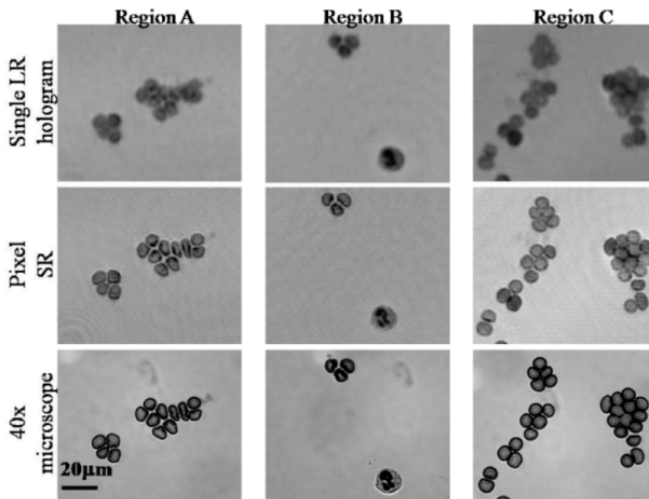

Figure 6: **Pixel SuperResolution and normal resolution reconstruction comparison.** *The effect of the Pixel SR algorithm can be easily observed also when studying reconstructions of images of a whole blood smear sample. Where the reconstructions using normal images are needing in quality, with finer details lost and smudged, the Pixel SR images are sharp, closing on the quality of a 40x optical microscope without the added bulk. Using the Pixel SR method even some sub-cellular structures can be observed [3].*

3.2 Cellphone digital holgoraphic microscope

First, we shall examine an extreme case of a low-cost high flexibility DHM device, build from a compact cellphone. Modern mobile phones have everything needed for an effective in-the-field diagnostics device, since they can capture images using their built-in cameras and send them into further analysis using a wireless internet connection. This has lead to a simple and inexpensive device shown in figure 7.

The main challenge in constructing an effective cellphone DHM is developing a method to effectively use its built-in camera. Most, if not all, cameras are of color variant, achieving color reproduction using

specially covered pixels for sensing light in red, green and blue parts of the visible spectrum. Selecting a partially coherent light source with well defined wavelength causes pixels to be unequally sensitive, thus an equalization step in the reconstruction process is needed. Furthermore, the overlap in the color spectrum of sensitive regions of the sensor is small, causing a low signal-to-noise ratio on some of the pixels. To remedy this, a special iterative algorithm that reconstructs the hologram in a full resolution of used imaging sensor was developed [2].
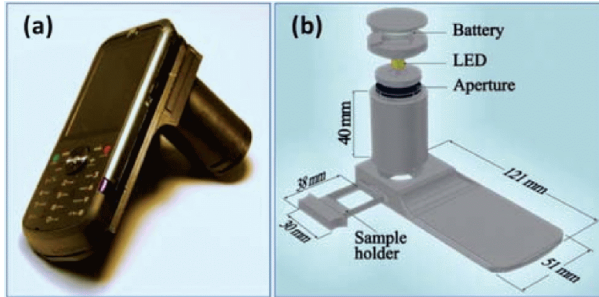

Figure 7: **Cellphone Digital Holography Microscope (DHM) setup.** *A simple, lightweight, inexpensive and highly portable lensfree microscope is shown. It operates on the basis of incoherent, in-line holography. The setup is extremely useful for performing fast, in-the-field measurements and examinations. The hardware weights approximately 38 grams, and uses only an inexpensive LED as a light source (≈ 587 nm). It has unit fringe magnification, thus using the whole active area of the sensor as its field of view [2].*

To fully understand the underlaying causes for necessary additional steps, we must first understand a standard, Bayer patterned sensor of a cellphone camera. Pixels of the sensor are covered by special color filters, so that independent pixels are sensitive only to some range of light wavelengths. For a color image reproduction, the color information from these filtered pixels is recovered, then the differences are smoothened in an approximate process called demosaicing, leaving a color variant of the recorded image [5].

The demosaicing algorithm developed by Tseng and coworkers [2] firstly equalizes green and red pixels, obtaining a good reconstruction of about 75% of the hologram. Missing blue pixels are then approximated from their neighbors and used for iterative refinement of the recorded hologram. At the final stage, the recovered hologram is digitally reconstructed, finally obtaining a microscopic image. The whole process is schematically illustrated in figure 8.
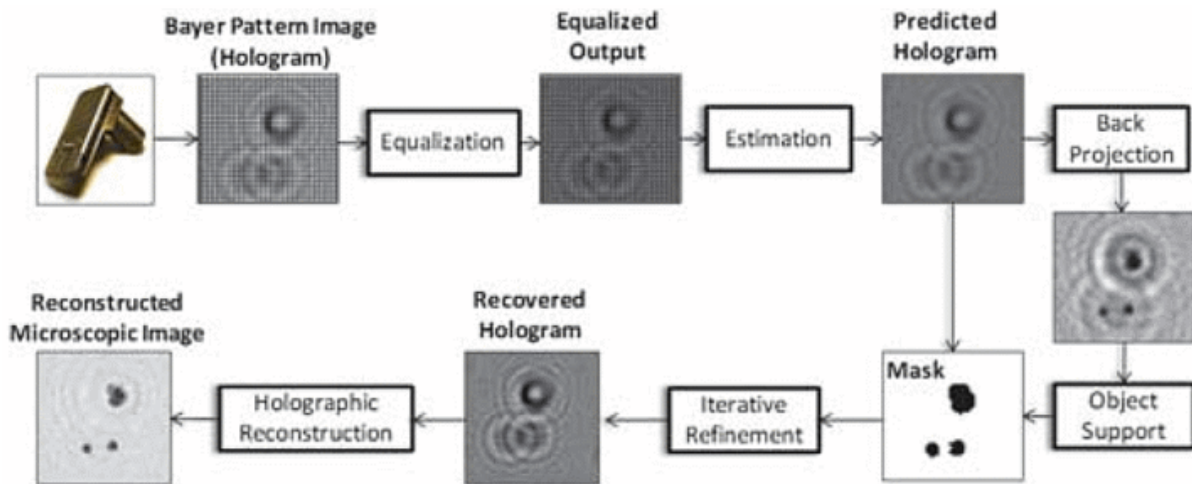

Figure 8: **Demosaicing algorithm.** *The image obtained from a cellphone lensfree microscope is marked by the Bayer pattern, as shown in the second frame. Red and green channels are then equalized, using a reference image recorded with the same light source as the hologram. Blue pixels, which have a small signal-to-noise ratio due to the color of the illumination LED, are then estimated from their neighbors, weighting average with the inverse values of the derivatives in the principal directions. Data for blue pixels is then further interpolated by masking the image in such a way that only areas with objects are modified. To refine the blue pixels algorithm reconstructs the image in the object plane and modifies it by removing the masked background. From this image a new hologram is calculated and compared to the measured one. The process is then repeated, modifying pixels in the unmasked area of the object, until a satisfactory match between the recorded and calculated hologram is achieved, thus obtaining refined values for the blue pixels [2].*

Comparison of reconstructions obtained form images recorded with the cellphone DHM and recordings captured using a classical microscope (Figure 9) shows that the quality is far from perfect. Sub-cellular structures, however, can still be resolved, which enables identification of particles in images, thus proving usability of this variant of the DHM [2].
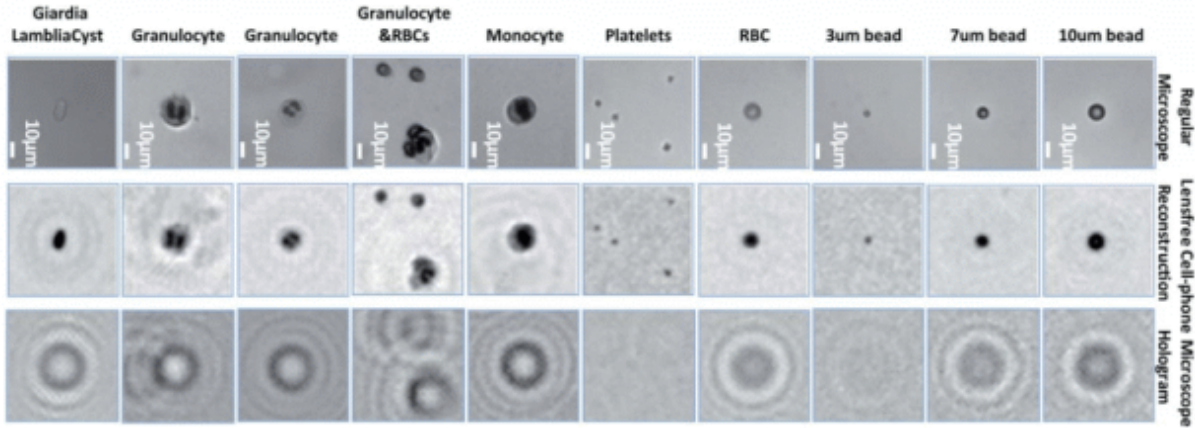

Figure 9: **Holograms and reconstructions using a cellphone DHM.** *Comparison of regular microscope and cellphone lensfree microscope images shows very good results, based on different samples, ranging in size from 3 to 10 μm, with visible sub-cellular structures [2].*

4   Examples of Applications

We shall confirm effectiveness and usefulness of DHM by studying three real-life applications and their results that were obtained in the recent years [6–8]. DHM has two main advantages which are illustrated in the examples below. Low manufacturing cost of devices based on cellphones and their large field of view are perfect for medical applications in developing countries, as illustrated by waterborne parasites detection [7]. Another useful application exploits the fact that DHM sensors can be integrated directly into a microfluidic device, giving rise to an automated leukocyte counting and classification device [6]. The third application uses primarily the DHM's high FOV to track trajectories of human sperms, uncovering previously unknown helical swim path trajectories [8].

4.1   Waterborne parasites detection

The first example uses cellphone DHM to detect and identify waterborne parasites. This process traditionally involved monitoring samples in a laboratory, thus making the water supply disinfection screening a rather demanding process [7].

Newly developed DHM can record images of water samples in sufficient quality to properly identify parasites in the sample. A map showing the results of such an automatic identification is shown in figure 10a. A great advantage of DHM is its large field of view (≈ 24 mm^2), which increases the count of detected parasites in highly diluted samples, thus enhancing the method's sensitivity. The high FOV and depth of field thus enables DHM to screen larger volumes of samples compared to traditional methods involving optical microscopes. Types of parasites are detected based on their physical characteristics, such as size, shape and presence of a flagella.

Because concentrations of parasites in the sample recorded in figure 10a were large ($\geqslant 10^6$/mL), the quality and the detection rate cannot be measured from that sample. To test the detection sensitivity of an automatic DHM, a sample of known concentration of the *Giardia Lamblia cists* was prepared, then diluted. At each step the automatically recorded concentration is noted (blue points in figure 10b) and compared to the concentration known from the sample preparation (gray line in graph 10b). The results show a good agreement and thus confirm a high sensitivity of the presented method.
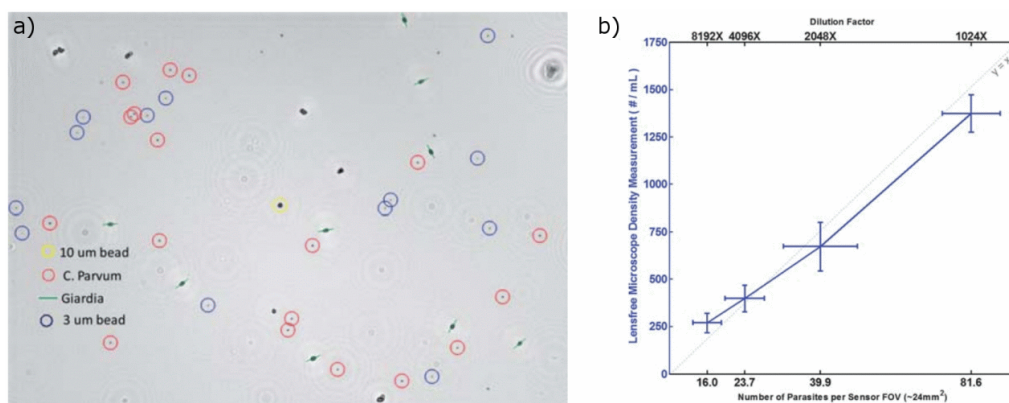
Figure 10: **Automatic identification of waterborne parasites.** *The identification of waterborne parasites depends on their characteristic shape and their phase image. Lensfree microscopy makes it possible to reconstruct the information about the amplitude and the phase of light on the reconstruction plane. Comparison of experimentally recorded data with known standard profiles enables the identification and counting of the parasites. Image a) shows the results of the identification of waterborne parasites in the studied sample. To test the accuracy of this method the sample is diluted and the measurement repeated several times. Results of such measurements are presented in figure b), showing a good agreement between known concentrations presented as the gray line and measured concentrations presented with blue points and linked with the blue line [7].*

4.2 Leukocyte counting and identification

Leukocyte counting and identification is an important factor in determining many medical conditions. One important marker is CD4/CD8 leukocyte ratio which is integral in identifying HIV infections [6]. Microfluidic in-flow detection of leukocytes has been problematic, but usage of imaging sensors embedded in microfluidic devices in tandem with DHM enables the building of inexpensive and effective microfluidic devices.
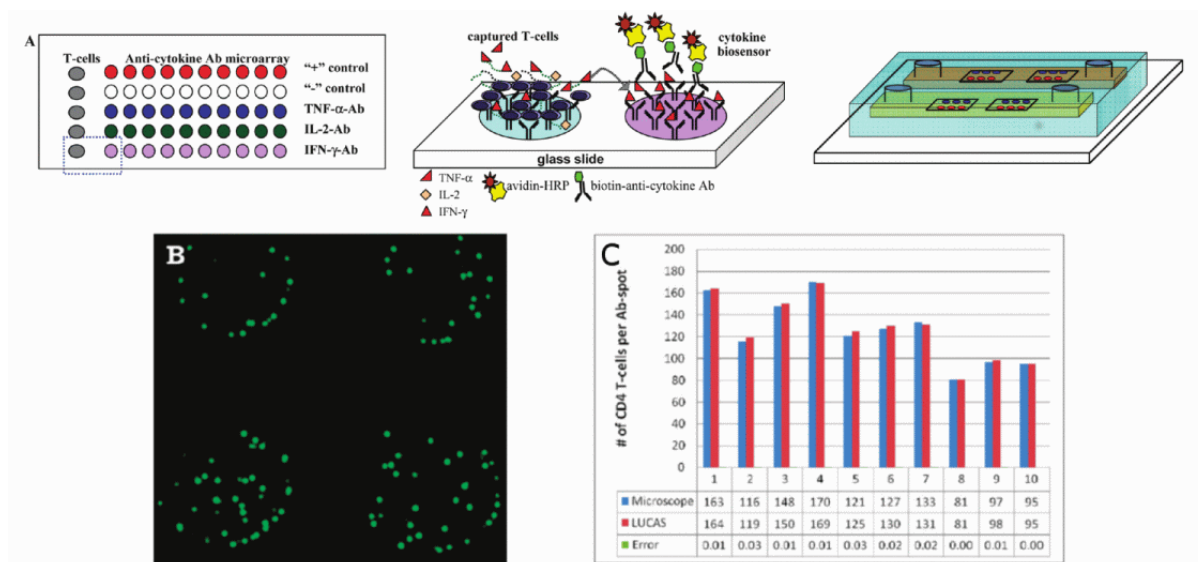

Figure 11: **On-the-chip ounting of leucotytes with a DHM.** *Figure A shows the setup used for the experiment. T-cell capturing spots are printed on a microarray in the vicinity of the antibody sensing spots, which can then be used to identify the leukocytes captured. The whole experimental assay is build using a microfluidic device to minimize the needed sample size. Figure B shows an image of captured leukocytes, recorded using a DHM device. It can be seen that individual leukocytes can be discerned and thus counted. To test this method, the results from automatic leukocyte counting were compared to traditional optical images. The comparison of these results is shown in figure C, revealing a very good agreement between both methods.*

Experimental devices are built by creating capturing spots and biosensing spots on a glass substrate. This substrate is then covered with PDMS microfluidic device and positioned on top of a CCD sensor for preforming DHM [6]. The whole setup is illustrated by Figure 11a.

Individual T-cells were visible during the experiment [6], but to confirm the cell phenotype, the captured cells were stained with fluorescent dies, thus combining DHM with fluorescence microscopy. The coloring of cells in image 11b can so be used to identify the type of leukocyes captured.

Confirming the T-cell identification, the next task was to test counting capabilities of the device. Numbers of detected cells per spot were collected for different samples and compared with results from a classical microscope. The results are presented in figure 11c above, showing an almost perfect agreement between both methods, with excess counts on the sides different methods, thus eliminating the question of a systematic error.

4.3   3D tracking of human sperms

Imaging of human sperms is difficult, due to the relatively large volume needed for trajectory tracking, in combination with the smallness of the sperm head, which requires a high magnification. This problem is ideal for DHM with its large FOV and relatively high magnification [8].

To monitor the position of human sperms in $3D$, two images in different color channels were taken at the same time. Both channels reference beams were offset by an angle, as depicted in figure 12 Al. This method allows for the reconstruction of the vertical coordinate of the sperm from different positions of its image in the hologram plane for both channels.

Monitoring the paths of human sperms in this way showed helical trajectories which are presented in Figure 12 right. Good resolution of the method and fast capture speed, combined with a uniquely large observed volume size, enabled the identification of four different types of swim paths [8].
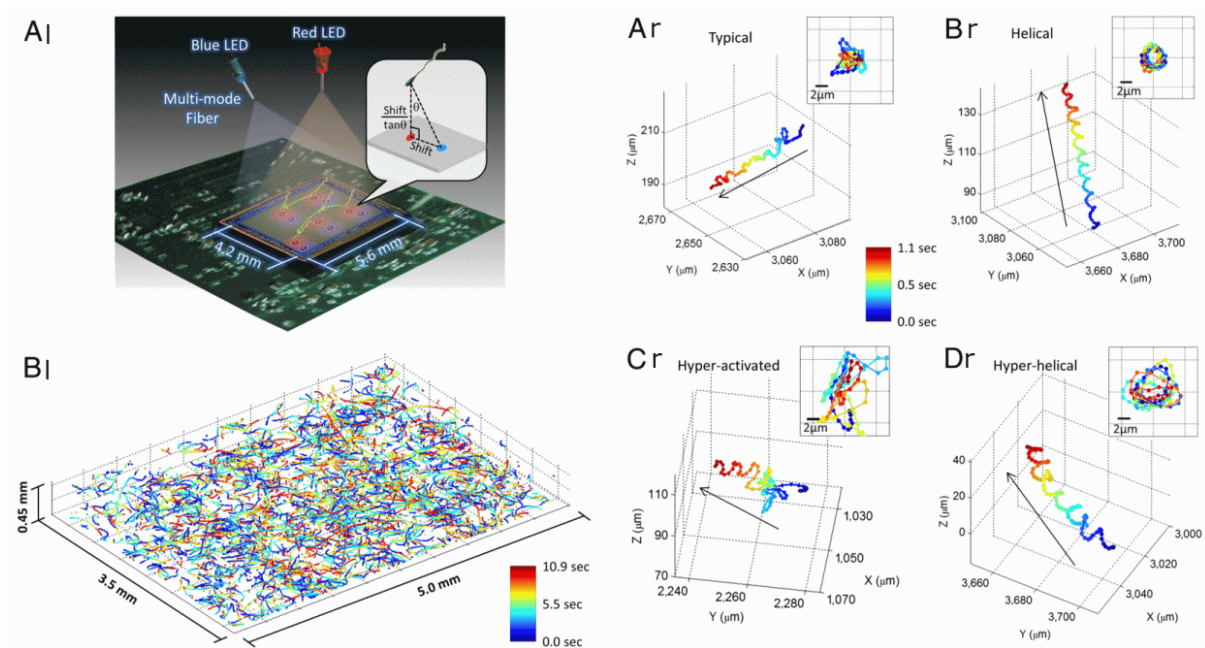

Figure 12: ***3D tracking dual color setup and recorded human sperms trajectories.*** *To record trajectories of sperms, their exact position in 3D has to be recorded. This is accomplished through recording of the position of the sperm heads in two different color channels, one being vertical and one being moved by a small angle (image Al). From these two illuminations it is possible to acquire two positions of sperms in two different projections. From their separation, the z coordinate of individual sperm can be calculated. Lensfree approach thus makes it possible to record trajectories of a large volume of sperms (image Bl) with sub-micron accuracy, revealing their helical trajectories, shown in the images to the right [8].*

5   Conclusion

We have presented the basics of digital hologram reconstruction, based mainly on the Fast Fourier transformation, which is an extremely effective numerical method. It has been demonstrated that the reconstruction is relatively simple, not demanding large amounts of computational power, and thus being highly available for general usage. It has also been shown that digital holograms pertain some properties of traditional holograms.

In the second part of the seminar we presented two different variations of digital holographic microscopy, one being capable of producing super resoluted images by bypassing the limiting factor of the pixel size, achieving much higher spatial resolution. In this way it is possible to obtain images of large areas (≈ 20 mm^2) with magnification and spatial resolution comparable to a 40x microscope objective, without added bulk of lenses in a traditional microscope. Another presented application takes a completely different approach, creating an inexpensive but effective microscope for in-the-field usage that can greatly improve diagnostic techniques in developing countries.

To illustrate the effectiveness of digital holographic microscopy or DHM, three real life examples were presented. These applications use many of the advantages DHM has to offer, from inexpensive in-the-field device application for waterborne parasites detection to employing the large volume scanning capability for tracking human sperms. The simplicity and portability of such devices is also illustrated by a microfluidic device with an embedded sensor for DHM, used to count and identify different types of leukocytes or T-cells.

As shown, digital holographic microscopy and digital holography in general are very active areas, with lots of promising applications. Another advantage of digital holography, not mentioned before, is the possibility to reconstruct phase difference in the reconstruction plane, which opens whole new areas of interference microscopy.

References

1. Haddad, W. *et al.* Fourier-transform holographic microscope. *APPLIED OPTICS* **31,** 4973–4978. ISSN: 0003-6935 (1992).

2. Tseng, D. *et al.* Lensfree microscopy on a cellphone. *LAB ON A CHIP* **10,** 1787–1792. ISSN: 1473-0197 (2010).

3. Bishara, W., Su, T.-W., Coskun, A. F. & Ozcan, A. Lensfree on-chip microscopy over a wide field-of-view using pixel super-resolution. *OPTICS EXPRESS* **18,** 11181–11191. ISSN: 1094-4087 (2010).

4. Schnars, U & Juptner, W. Digital recording and numerical reconstruction of holograms. *MEASUREMENT SCIENCE & TECHNOLOGY* **13,** R85–R101. ISSN: 0957-0233 (2002).

5. Wikipedia. *Bayer filter — Wikipedia, The Free Encyclopedia* [Online; accessed 15-December-2014]. <\url{http://en.wikipedia.org/w/index.php?title=Bayer_filter&oldid=636888675}>.

6. Stybayeva, G. *et al.* Lensfree Holographic Imaging of Antibody Microarrays for High-Throughput Detection of Leukocyte Numbers and Function. *ANALYTICAL CHEMISTRY* **82,** 3736–3744. ISSN: 0003-2700 (2010).

7. Mudanyali, O., Oztoprak, C., Tseng, D., Erlinger, A. & Ozcan, A. Detection of waterborne parasites using field-portable and cost-effective lensfree microscopy. *LAB ON A CHIP* **10,** 2419–2423. ISSN: 1473-0197 (2010).

8. Su, T.-W., Xue, L. & Ozcan, A. High-throughput lensfree 3D tracking of human sperms reveals rare statistics of helical trajectories. *PROCEEDINGS OF THE NATIONAL ACADEMY OF SCIENCES OF THE UNITED STATES OF AMERICA* **109,** 16018–16022. ISSN: 0027-8424 (2012).